



# Analysis and modeling of the aerodynamic ceiling effect on small-scale propellers with tilted angles



Yiliang Liu<sup>a</sup>, Zi Kan<sup>a</sup>, Huadong Li<sup>a</sup>, Yuzhe Gao<sup>a</sup>, Daochun Li<sup>a,b</sup>, Shiwei Zhao<sup>a,\*</sup>

<sup>a</sup> School of Aeronautic Science and Engineering, Beihang University, Beijing 100191, China

<sup>b</sup> Tianmushan Laboratory, Yuhang District, Hangzhou 311115, China

## ARTICLE INFO

### Keywords:

Unmanned aerial vehicles

Ceiling effect

Cfd

Propeller

## ABSTRACT

Micro air vehicles with propellers have been widely used in military and civilian applications due to their high maneuverability and low cost. As the mission scenarios and requirements of rotorcrafts become more complex, proximity effects caused by confined environments, such as the ceiling effect cause significant interference to the performance and stability of rotors. Most researchers have analyzed this phenomenon by considering the ceiling effect in hover conditions. However, few scholars considered the tilt angle between the rotor and the ceiling, which is more likely to occur in real missions, such as the close inspection of bridges or large equipment, flight in narrow indoor environments, and flight near the ceiling for fully actuated multirotors. In this study, a CFD-based study is conducted to evaluate the ceiling effect for small-scale tilted propellers. The aerodynamic analysis was experimentally evaluated through a series of ground tests in a test bench designed for this research. The CFD results were validated by a mesh-independent study and experimental data comparison. The results show that in contrast to the phenomenon of reduced thrust when tilt angles exist between the rotors and ground, the existence of tilt angles between the propeller and the ceiling reduces the thrust-increasing effect of the ceiling when the dimensionless distance is greater than 0.6. When the distance gets smaller, the thrust-increasing effect increases when the tilt angle is greater than 10°. In particular, when the distance is less than 0.3, the existence of tilt angles will increase the thrust-increasing effect of the ceiling. Additionally, a data-driven model has been proposed to predict the thrust with the distance to the ceiling and the angle inclination between the rotor and the ceiling. This model enables future rotorcrafts that require accurate models to operate in narrow environments.

## 1. Introduction

UAVs (unmanned aerial vehicles) and MAVs (micro air vehicles), which are compact and have high maneuverability and low manufacturing costs, have been rapidly developed for military and civilian applications [1]. In recent years, with the development of sensing technology, electric propulsion, and data processing [2,3], drones can complete complex tasks in a variety of scenarios. Due to their small size and flight capabilities, drones can maneuver through tight spaces and are not restricted by terrain and other conditions. Typically, these special aircraft have been widely used in reconnaissance, exploration, rescue, agriculture, and other fields, saving considerable manpower and material resources. However, a large number of new applications for drones are needed in modern society such as the inspection and maintenance of large equipment, complex indoor environment mapping and rescue, and long-endurance drones that rely on

walls to improve hover efficiency and other manipulation operations [4] require rotorcrafts to operate in narrow corridors close to obstacles that are inaccessible to conventional vehicles. Since micro drones are inherently unstable because of their small size and low speeds [5,6], floors, walls, and ceilings [7] of these environments constrain the free development of the flow field and affect propeller performance [8], destabilize the rotorcrafts and cause serious safety risks.

Previous research has shown that the effect of lateral walls on the thrust of the rotor is negligible [9]. Thus, studies on the proximity effect are conducted to mainly focus on the ground and ceiling effects. It is well known that rotors experience significant aerodynamic interactions when rotating close to the ground. The ground effect was discovered in helicopter studies in the 1930s [10]. Later, Cheeseman and Bennett [11] used blade element theory to model the change in thrust generated by a propeller rotating close to the ground under different distances. Their model has been widely used and has become a standard model because it

\* Corresponding author at: Dr. Shiwei Zhao, Beihang University School of Aeronautic Science and Engineering, China  
E-mail address: [shiweizhao@buaa.edu.cn](mailto:shiweizhao@buaa.edu.cn) (S. Zhao).

can quickly predict the thrust changes of propellers under the influence of ground effects. Afterward, scholars established various models of ground effects based on different methods. Xin [12] studied the characteristics of the inflow for rotors at different heights above an inclined ground and modeled them. Different inclinations of the ground were considered and the asymmetry phenomenon of the rotor wake was found. With the development of MAVs in recent years, research on the ground effect of small-scale propellers [13,14] has become more popular and the tilted ground effect often encountered in actual flight missions has received widespread attention. Reference [15] analyzed the evolution of the rotor wake of a hovering rotor operating under ground effects above parallel and inclined surfaces, and compared the experimental measurements and results of the numerical simulations. Milluzzo [16] analyzed the flow field of a rotor hovering above inclined surfaces at angles from 0° to 30° by PIV experiments. They found that the wake structure was sensitive to the ground plane angle, and that the radial distribution of the axial velocity through the rotor changes with the ground plane angle. Garofano-Soldado [17] conducted CFD simulations and experiments to investigate the ground effect on small-scale tilted propellers and proposed a new model to predict the changes in thrust when a rotor hovers above the ground with tilt angles. They found that the thrust generated by the rotor decreases when the tilt angle increases. Rovere [18] used the CFD method to simulate the outwash generated by a micro-rotor operating under a ground effect and analyzed its safety.

Although the ceiling effect has not been analyzed in helicopter research [19], it has a significant impact on drones operating in restricted environments. The ceiling effect can help UAVs save energy by increasing thrust. In addition, it will cause drones to be closer to ceilings, where may result in collisions. The first known research on the ceiling effect was presented in [20], Rossow documented the thrust of rotors that are affected by both the ground and ceiling effects. In the last decade, related research on rotors under ceiling effects has received more attention and has become further developed [21]. Sanchez-Cuevas [22] measured the change in thrust of a quadcopter under the influence of the ceiling effect and applied it to a bridge inspection aircraft. The results show that making use of the ceiling effect will improve the maximum flight time of the drone. Conyers [23] used blade element and momentum theory to empirically analyze the impact of the ceiling effect on small-scale propellers and compared it with that of the ground effect. Hsiao and Chirarattananon [24] discovered that the quadrotor can save considerable power when it flies close to the ceiling plane. Then, they proposed a model to predict the increased thrust near the ceiling by blade element momentum theory [25]. Afterward, some new models have been proposed by analytical and experimental studies, and the benefits of the ceiling effect are explained in detail [26,27]. Carter [19] conducted PIV experiments on the three proximity effects of the quadrotor and evaluated classic ground and ceiling effect models. Then, they demonstrated distribution changes of the flow field under the influences of the ground and ceiling effects and conducted simulation analysis on safety. Furthermore, they established a reduced-order model and analyzed the safety implications of near-ground/ceiling flight. Hao [28] conducted numerous investigations of hovering micro revolving wings under ground and ceiling effects, especially for very close distances. They found that the ground effect is more helpful increasing the thrust and that the ceiling effect is more beneficial for high aerodynamic efficiency. Cai [29] used experimental methods with different sizes and shapes of planes to analyze the partial ground and partial ceiling effect on the propeller performance and found that the main cause of the changes in the thrust is the area of the ground-plate and not its shape. In fact, in actual flight missions, there are rarely situations where the rotor disk is completely parallel or perpendicular to the wall (ground, ceiling, and sidewall), such as a rotor operating near an inclined wall or ceiling, moving near a ceiling or ground in a certain attitude, and a fully-actuated drone hovering near a wall. Although the three proximity effects of propellers were extensively examined in previous works, few scholars have focused on analyzing propellers that are tilted relative to a

ceiling.

In this study, the ceiling effect of tilted small-scale propellers is described. To date, no ceiling effect model has been proposed under inclined ceiling conditions. To contribute to the growth in the field of UAVs, we analyzed and quantified the ceiling effect on a tilted propeller that may occur when complex tasks in a narrow environment are performed. The rest of the paper is organized as follows: In Section 2, the propeller that we used, the numerical calculation methods, and the experimental devices are introduced. In Section 3, the experimental and independent validations of the CFD method are presented. In Section 4, the thrust changes under the ceiling effect with tilted rotors and the causes of these phenomena are analyzed. In Section 5, a data-driven ceiling effect model is proposed and implemented for several propellers. In Section 6, concludes and future perspectives are provided.

## 2. Methodology

### 2.1. Geometric model

The object of study of this article is a T-Motor propeller, type '13 × 4.4'. The investigated propeller, as illustrated in Fig. 1(a) is a carbon fiber propeller with two blades. The diameter and pitch of the propeller are  $D=330.2$  mm (13 inches) and  $P=111.76$  mm (4.4 inches) respectively. Fig. 1(b) displays the 3D geometry of the propeller used in the numerical simulation, which was modeled by a three-dimensional scanner (DUUMM BASIC) with an error of less than 0.03 mm. Fig. 2 shows the length of the chord and the pitch of the airfoil for different locations of the propeller along the span of the blade. The pitch angle varies from 5° to 23°. The chord length is at 3/4 of the radius location. Fig. 3 shows the blade section at 3/4 of the radius location. As shown in the picture,  $\alpha = \beta - \varphi$  is the angle of attack of the airfoil, which represents the pitch angle of the section and  $\varphi = \tan^{-1}(U_n / U_t)$  is the downwash angle.  $U$  represents the resultant velocity of the flow, which has two components, the normal velocity ( $U_n$ ) and tangential velocity ( $U_t$ ). No other motion occurs in the propeller except for the rotation around the shaft. Hence the normal velocity only depends on the induced velocity of each section.

It is known that the Reynolds number at 3/4 of the radius location of the blade influences the propeller performance the most [30]. In this study, the Reynolds number value of most cases is approximately 100,000. The propeller is rotating at a low Reynolds number, and a large number of sections of the blade are in the stall state. Under this condition, the Coriolis effects may delay the separation on the surface of the blade [31].

In addition, two other small-scale propellers were used in the ground experiment. These propellers are T-Motor '10 × 3.3' and APC '11 × 4.7' (see Fig. 4). Two propellers were tested under selected conditions with different distances to the ceiling and tilted angles (see Table 1) to validate the ceiling effect model and assess its accuracy and universality. The vertical distance between the ceiling plane and the center of the disk is defined as  $l$ , the radius of the propeller is defined as  $R$ , and the tilt



Fig. 1. Real and 3D geometric model of T-Motor propeller- 13 × 4.4.

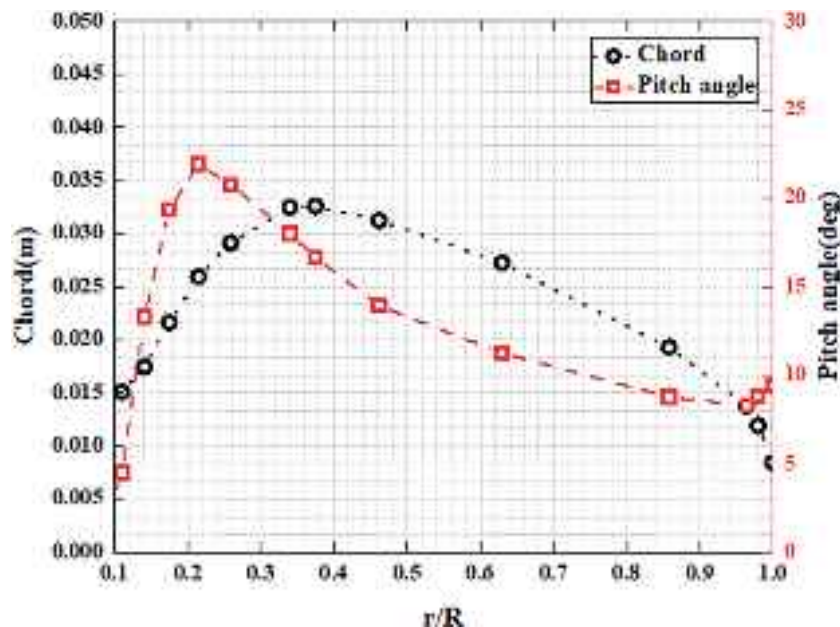


Fig. 2. Blade chord and pitch angle distributions of T-Motor propeller- 13 × 4.4.

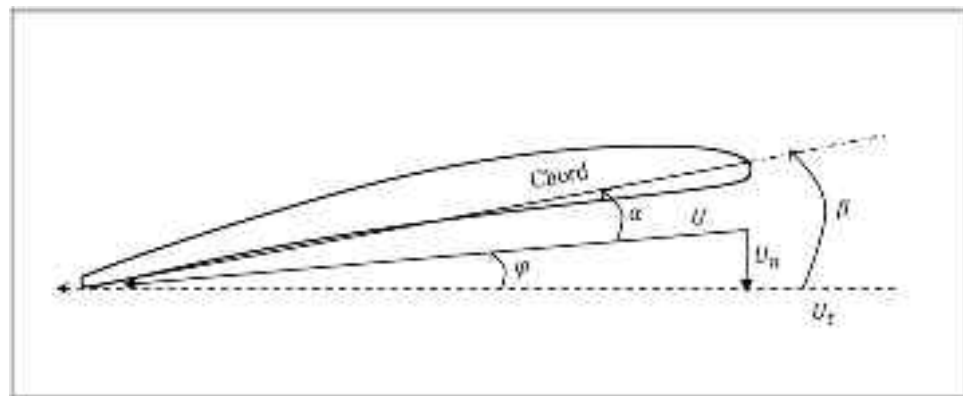


Fig. 3. Blade section at 3/4 of the radius of the blade.

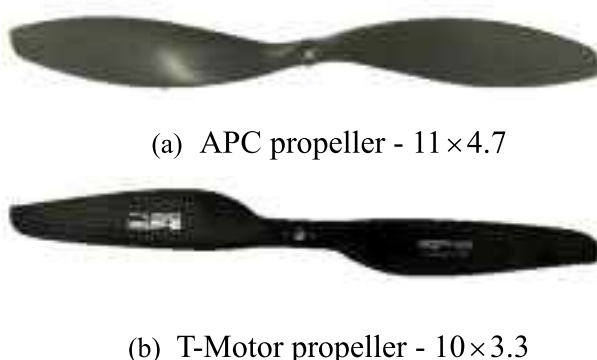


Fig. 4. Propellers used to validate the proposed model.

angle is defined as  $\theta$ .

## 2.2. Domain division and computational mesh

A diagram of the computational domain used to simulate the ceiling effect with a tilted propeller was displayed in Fig. 5. The entire

**Table 1**

Test conditions of the other two propellers (APC - 11 × 4.7 and T-Motor - 10 × 3.3).

Propeller	Test conditions
APC propeller - 11 × 4.7	$\theta = 0^\circ, l/R = 1.5, 1.2, 1.0, 0.8, 0.6, 0.5, 0.4, 0.35, 0.3, 0.2$ $\theta = 5^\circ, l/R = 1.5, 0.5, 0.3$ $\theta = 10^\circ, l/R = 0.8, 0.35$ $\theta = 15^\circ, l/R = 1.2, 0.4$ $\theta = 20^\circ, l/R = 0.6$ $\theta = 25^\circ, l/R = 1.0$
T-Motor propeller - 10 × 3.3	$\theta = 5^\circ, l/R = 1.5, 0.5, 0.2$ $\theta = 10^\circ, l/R = 0.8, 0.4, 0.3$ $\theta = 15^\circ, l/R = 0.6$ $\theta = 20^\circ, l/R = 1.2$ $\theta = 25^\circ, l/R = 1.0$

computational domain is composed of two parts: a rotating domain and a static region. The external static domain is a cylinder with a diameter of 20R and a height of 24R. The rotating domain is also a cylinder enclosed in the propeller with a diameter of 1.06D and a height of 0.2D. These two domains are linked by three pairs of interfaces to transfer data. To capture the flow characteristics near the blades, an invisible

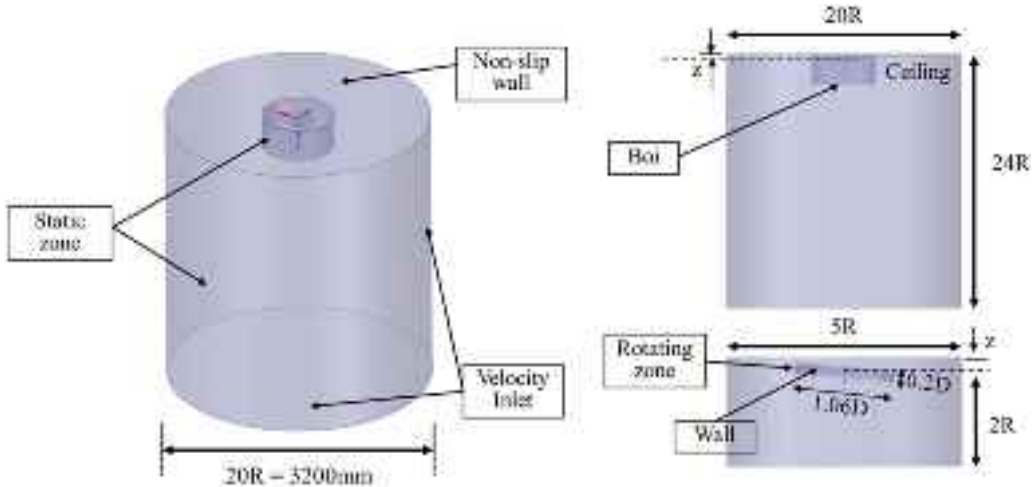


Fig. 5. The computational domain and boundary conditions.

region Boi (Body of influence) is set up, in which the size of the volume meshes is restricted to be sufficiently small. In the rotating domain, the propeller rotated at a rotational speed of 5000 rpm to stimulate the flow. The rotating domain and the propeller are at an angle with respect to the ceiling. For different cases, the positions, attitudes of the propeller, and rotating domain change for every  $l$  and  $\theta$  value, and the geometry and mesh are rebuilt accordingly, leaving the rest of the parameters unchanged. To ensure the resolution ratio of the mesh and speed up the calculations, poly grids were constructed, which are currently widely used to analyze aerodynamic characteristics. Fig. 6 shows the section of the computational mesh, especially the mesh details near the blade surface. The  $y^+$  values at the chord of the propeller at 3/4 radial position and the ceiling both satisfy:  $y^+ < 1$ . The mesh quality was able to satisfy the simulation requirements. The total number of mesh elements was approximately 449 million, including 382 million for the rotating domain and 66 million for the static domain.

### 2.3. Computational method

Many researchers have used CFD to analyze the performance of different propellers and recognize the mechanisms of the flow [13,17, 21]. Since the blade tip Mach number is less than 0.4 when the blade

rotating speed is 5000 rpm, the flow can be regarded as incompressible. Thus, we chose the finite volume method for simulation investigations, where the Reynolds-Averaged Navier-Stokes (RANS) equations are solved. The fluid is assumed to be incompressible and the body force is neglected.

According to the previous literature [32], three major CFD methods are used to simulate rotating propellers: the multiple reference frame (MRF) method, the sliding mesh method, and the overlapping grid method. The first is a steady-state method and the other two are transient simulations. The MRF approach and sliding mesh method divide the domain into a stationary zone and a rotational zone. They both transfer information by the matched interfaces, although the former applies the equations in a stationary frame with rotational axes and the other regards the propeller as a dynamic object and provides time-dependent solutions. The overlapping grid method also allows the propeller to rotate, the difference is the computational domain and the way it transfers the parameters. Usually, the solution of the MRF method is applied as the initial condition of the sliding mesh method. Although transient techniques often offer better simulations, the cost is extremely high, especially when the number of calculations is large.

The focus of this work is the propeller performance under different conditions. Therefore, in this paper, we used the MRF method due to its

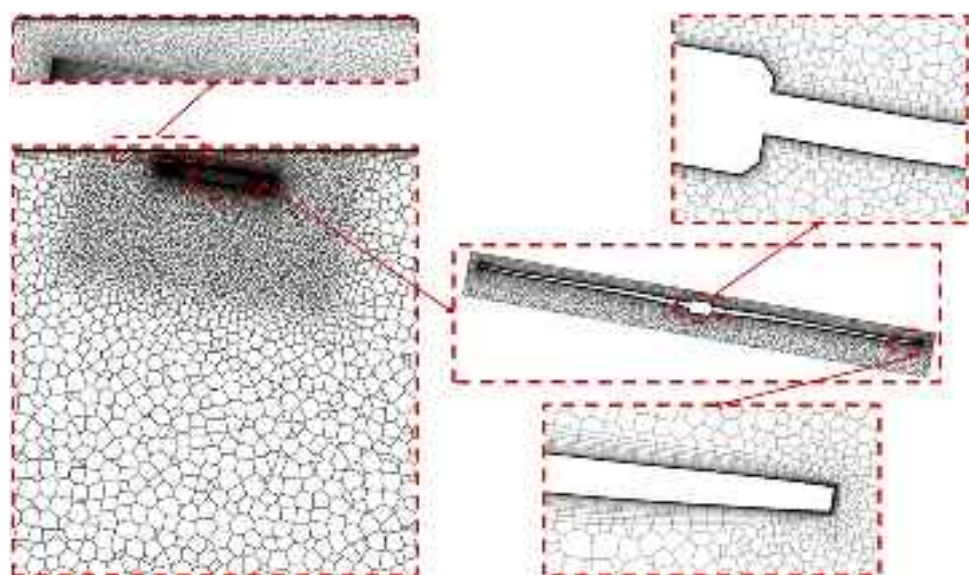


Fig. 6. Computational mesh.

efficiency and accuracy. Due to the Mach number at the blade tip being much less than 0.3, the flow was assumed to be incompressible, and the pressure-based solver [33,34] wherein the constraint of mass conservation of the field is achieved by solving a pressure equation was chosen. In the Reynolds-Averaged Navier-Stokes method, averaging procedures are applied to the N-S equation and the transport equations in the RANS model need to be solved in the turbulence model [35]. The popular  $k-\omega$  SST (shear stress transport) turbulence model [36], which combines the advantages of both the  $k-\epsilon$  model in the far field and the  $k-\omega$  model close to the wall, was adopted. This turbulence model has been widely used for similar applications for the propeller [17,37]. The  $k-\omega$  SST model incorporates two equations, which describe the evolution in time of the turbulent kinetic energy and the specific dissipation rate. The coupled algorithm [33,34] is used in this paper to solve the continuity equation and momentum equation simultaneously to improve the rate of solution convergence and the second-order upwind scheme is used to improve the accuracy of the simulations.

The boundary conditions for the calculation of the ceiling effect of a propeller with a tilted angle are applied according to Fig. 5. In the rotating domain, the blades are set as moving walls with no velocity. In the static domain, the ceiling is set as a non-slip wall and the remaining far-field boundaries are defined as a velocity inlet where the velocity value is set to 0 m/s. Three pairs of interfaces that separate the two domains are matched. The propeller rotating speed is  $\omega = 5000$  rpm.

The angles simulated by CFD were: 0°, 5°, 10°, 15°, 20°, 25°, and 30° and dimensionless distances were  $l/R = 2, 1.5, 1.2, 1, 0.8, 0.6, 0.5, 0.4, 0.35, 0.3, 0.25$ , and 0.2. As the distance from the rotor plane to the ceiling decreases, the blade will interfere with the ceiling. Therefore, the change in the angle will be limited when the blade is close to the ceiling.

#### 2.4. Validation of the mesh independence

To exclude the effect of the mesh resolution on the CFD results, a mesh independence verification was conducted. To ensure generaliz-

ability, we chose the case with a 10-degree tilted angle and a distance of  $l = 0.5R$ . The purpose of this section is to find a mesh that results in an acceptable computational time, high accuracy of calculation results, and good convergence of the solution residuals. In this process, four meshes with different sizes were generated for comparison. From Mesh 1 to Mesh 4, the surface mesh size of the propeller, the cell size of the leading and trailing edge of the blade, and the mesh size on the surface of the matched interfaces have gradually increased. The propeller surface meshes in all four meshes satisfy the  $y^+$  values of approximately 1. Fig. 7 displays the surface grid of the rotational domain for four different meshes, the details of which can be seen in Table 2. As is shown in the picture, Mesh 1 is coarser than others with 118 million elements, while Mesh 2 and Mesh 3 are denser with 327 and 450 million elements, respectively. Mesh 4 has the greatest number of elements at 522 million. The unstructured meshes were refined based on the curvature and scale of the propeller surface in all cases. As is displayed in Fig. 8, starting from Mesh 3 with 4,497,301 elements, the simulation results hardly change. Therefore, Mesh 3 is used for calculations in the following chapters.

#### 2.5. Experimental setup

To verify the CFD results, we used bench experiments in the intelligent drone lab of Beijing University of Aeronautics and Astronautics. Fig. 9 shows a schematic diagram of the ground test system. The bench

**Table 2**

Number of elements of the four meshes.

Serial number		Rotating domain	Stationary domain	Total
Mesh 1	Cells	986,309	193,283	1179,592
Mesh 2	Cells	3054,835	212,237	3267,072
Mesh 3	Cells	3829,398	667,903	4497,301
Mesh 4	Cells	4526,144	693,524	5219,668

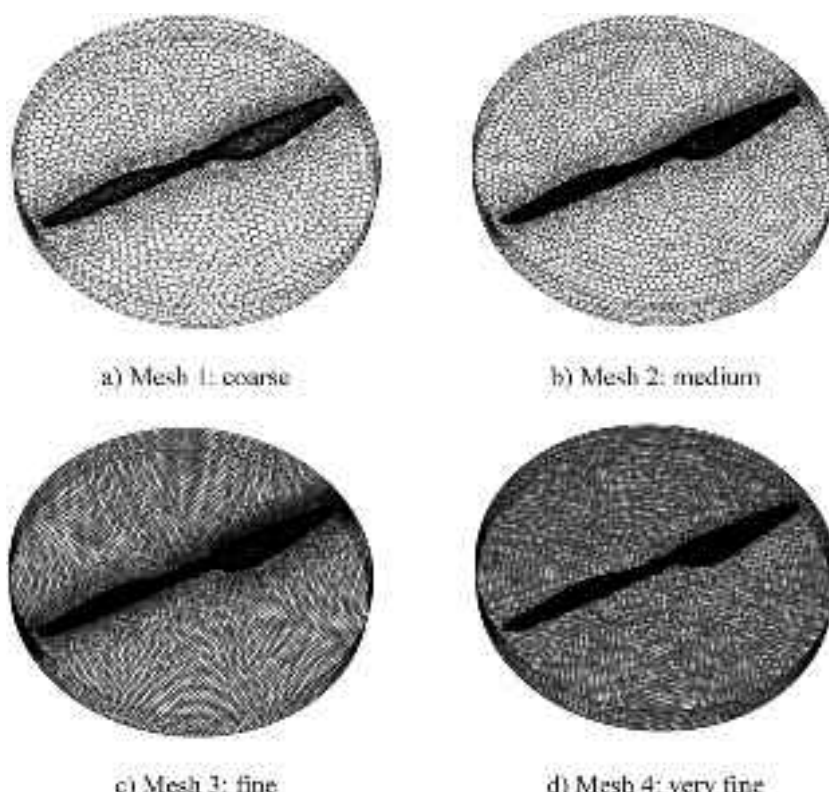


Fig. 7. Definition of the four meshes.

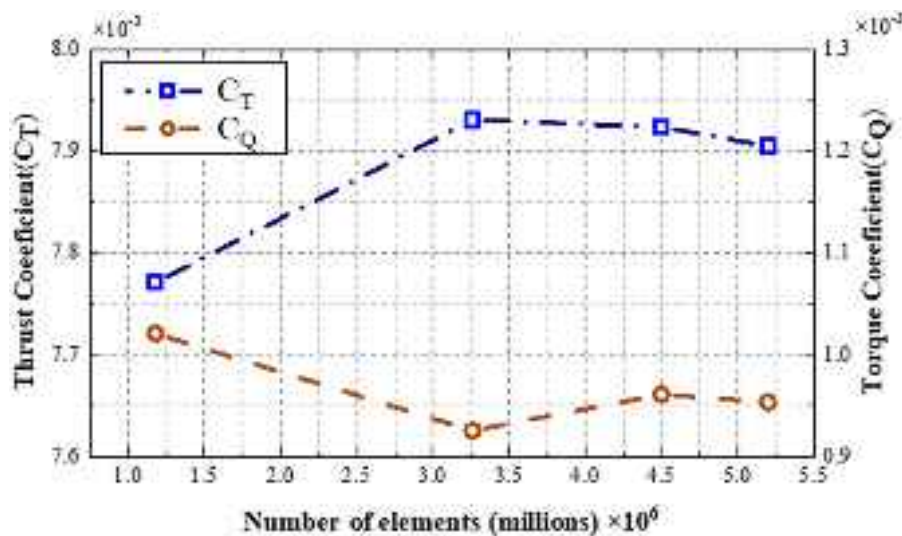


Fig. 8. Thrust coefficient versus number of elements.

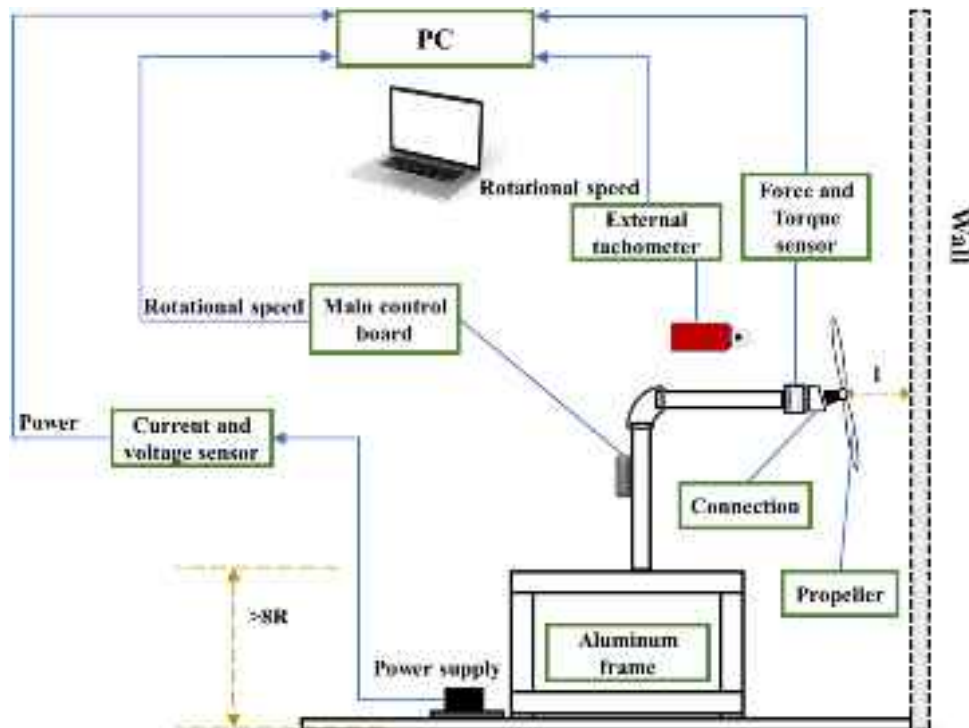


Fig. 9. Schematic diagram of the ground test.

was made up of an aluminum structure, and includes the tested propeller, the connection with a tilted angle, the data acquisition device, the power supply system, and the sensors and controllers. An FC6D50 force/torque sensor was applied to the tilted connection. This sensor can measure the six components of the force and torque with accuracies of  $1/10\text{ N}$  and  $1/100\text{ Nm}$ , respectively. The measuring range is  $100\text{ N}$  for the z force,  $50\text{ N}$  for the x and y forces, and  $10\text{ Nm}$  for T. The testing frequency is  $500\text{ Hz}$ . Fig. 10 shows the composition of the entire ground test bench.

A customized electric board is used to control the motor. A microprocessor control circuit based on an arm cortex architecture is used to control the speed in a non-contact manner, and an integrated level comparator is used to determine the frequency of the change in the reverse electromotive force of the motor rotation, which in turn converts

the rotational speed. The electronic speed controller uses PWM wave control, which is generated by the PWM pin of the microprogrammed control unit, and performs real-time and accurate tracking control of the speed command by closing the speed to the control logic and using the control method with feed-forward and feedback.

Unlike traditional ceiling effect analysis which considered only the distance from the rotor plane to the ceiling and the size of the propeller [19], our study incorporates the relative angle between the rotor plane and the ceiling as a variable. Fig. 11 shows the adapting pieces made by a 3D printer that were used to change the relative angle ( $\theta$ ). A total of 94 experiments have been carried out, including 29 cases for the other two propellers, as mentioned above. Three different tests were taken in each measurement to take the mean value and reduce the error that occurred during the experiment. The data acquisition process took 100 s for each

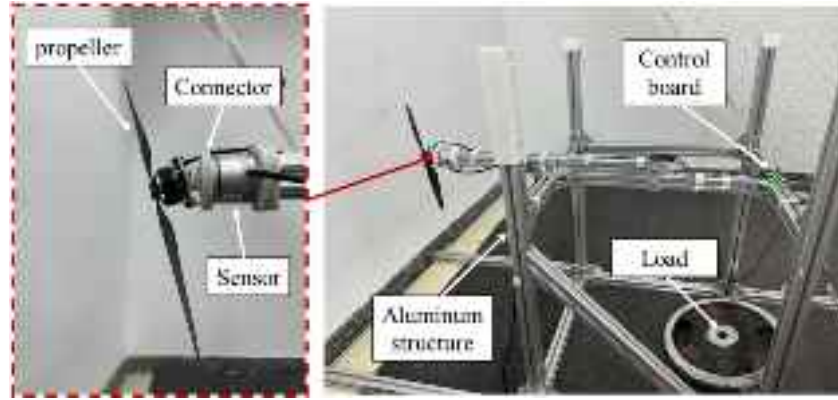


**Fig. 10.** Test bench to study the ceiling effect with tilted propellers.



**Fig. 11.** Connectors for different tilt angles (starting from the left side of the first row, they are  $\theta = 0^\circ, 5^\circ, 10^\circ, 15^\circ, 20^\circ, 25^\circ, 30^\circ$ ).

measurement. First, the rotor was controlled to rotate at the aimed speed for 15 s. Second, the force and torque values were recorded for 15 s. Then, the propeller rotating speed was controlled to 500 rpm for 40 s. Finally, the motor was switched off for 30 s. All experimental data were collected in the sensor reference frame and the corresponding values were projected to the disk coordinate system.

#### 2.6. Modified hsiao and chirarattananon's ceiling effect model

In this paper, Hsiao and Chirarattananon's ceiling effect model [25] was modified to predict the thrust of small-scale rotors hovering with angles of inclination to the ceiling under the ceiling effect. Hsiao and Chirarattananon used blade element momentum theory and a control volume analysis to model the ceiling effect. They assumed that the air is incompressible, the flow through the rotor disk is uniform and the flow through a control volume above the rotor disk is horizontal. In their theory, they did not consider the viscosity and rotationality. They regarded the symmetry of the system and the interaction between adjacent propellers as two primary factors and used two dimensionless coefficients to describe the asymmetry flow and wake recirculation for the quadrotors. They found that the presence of the ceiling decreases the downwash velocity near the rotor plane and the rotor thrust significantly increases near the ceiling. Their model is as follows:

$$\gamma(\delta, \alpha_0, \alpha_1) = \frac{1}{2} (1 - \alpha_1 \delta^2) + \frac{1}{2} \sqrt{(1 - \alpha_1 \delta^2)^2 + \frac{\alpha_0 \delta^2}{8}} \quad (1)$$

where  $\gamma$  is the dimensionless ceiling coefficient  $T_{ICE}/T_{OCE}$ ,  $T_{ICE}$  is the thrust when the propeller is affected by the ceiling, and  $T_{OCE}$  is the thrust when the propeller is not affected by the ceiling,  $\alpha_0$  is an empirical coefficient representing the induced velocity angle caused by surround-

ings,  $\alpha_1$  is an empirical coefficient representing the interaction between the propellers that are caused by the presence of a ceiling, and  $\delta$  is the propeller-to-ceiling ratio  $\delta = R/D$ ,  $R$  is the propeller's radius and  $D$  is the propeller-to-ceiling distance. When there is only one propeller and the rotor plane is parallel to the ceiling,  $\alpha_0$  equals 1 and  $\alpha_1$  equals 0.

Due to the accuracy of Hsiao and Chirarattananon's theory, a modification of their theory that includes the consideration of the rotor tilt angle is proposed. Since our research object is a single propeller, there is no interference from other nearby propellers. Additionally, from the flow field visualization from the following chapter, it can be found that no obvious recirculation phenomenon occurs. For these reasons, the coefficient  $\alpha_1$  can be ignored. We used a function  $f_t(\theta)$  to replace the coefficient  $\alpha_0$  in Eq. (1), the thrust ratio can be expressed as follows:

$$\frac{T_{ICE}}{T_{OCE}} = \frac{1}{2} + \frac{1}{2} \sqrt{1 + \frac{1}{8(l/R)^2} f_t(\theta)} \quad (2)$$

It is assumed that Eq. (2) should be close to the theory predicted by Hsiao and Chirarattananon when  $\theta = 0^\circ$ . Due to the existence of tilt angles between the ceiling and the rotor plane, the function  $f_t$  can't be ignored. The proposed model makes certain modifications to the classic theory for small-scale propellers. Based on previous works, Chen [38] organized different inflow models for propellers. The outcomes of the first harmonic inflow models were confirmed to fit well with the experimental results. Garofano-Soldado [17] used the inflow model to develop the tilted ground effect model. According to this line, the function  $f_t$  is defined as follows:

$$f_t(\theta) = a_0 + \sum_{n=1}^{\infty} a_n \cdot \sin(n\theta) + \sum_{n=1}^{\infty} b_n \cdot \cos(n\theta) \quad (3)$$

Since the first harmonic is accurate enough, the thrust ratio depends

on the distance  $l$  (the vertical distance between the ceiling plane and the center of the disk) and the tilt angle  $\theta$  can be expressed as follows:

$$\frac{T_{ICE}}{T_{OCE}} = \frac{1}{2} + \frac{1}{2} \sqrt{1 + \frac{1}{8(l/R)^2} (a_0 + a_1 \sin \theta + b_1 \cos \theta)} \quad (4)$$

where the values for the coefficients  $a_0$ ,  $a_1$ , and  $b_1$  will be derived from numerical simulations for the T-Motor propeller. These values will be provided in the subsequent [subSection 4.3](#).

### 3. Validation

#### 3.1. Comparison of the mrf and sliding mesh method

In this paper, we used the MRF method due to its efficiency and accuracy. MRF method is a steady-state approximation method and maintains the rotor in a fixed position within a moving reference frame. Due to the presence of tilted ceilings in this research, changes in blade position relative to the ceiling may affect the thrust of the propeller. Therefore, we use the sliding mesh method to verify the accuracy of the MRF method.

The case same as the validation of the mesh independence ( $l = 0.5R$ ,  $\theta = 10^\circ$ ) was considered. Additionally, the hover case was also calculated for comparison. The results of the MRF method served as the input for transient simulation, and the sliding mesh method was developed to simulate the unsteady flow. The time step was set to  $\Delta t = 0.000033s$ , corresponding to the rotation angle per step of  $1^\circ$ . The calculations converge after fifteen revolutions. The thrust ratio  $T_{ICE}/T_{OCE}$  is used to compare the results. [Fig. 12](#) shows the changes in thrust at different blade positions in almost one revolution and the horizontal axis  $t^*$  represents the number of time steps. As the results show, although the existence of the inclined ceiling causes large fluctuations in thrust when the blades rotate to different positions, the average value of  $T_{ICE}/T_{OCE}$  changes is very little, and the error between the two methods is only 0.43 %. The results in this section show that the MRF model can accurately predict the propeller thrust when the propeller is affected by the inclined ceiling.

#### 3.2. Comparison of the propeller performance

For verification purposes, we compared the experimental and calculation results of the propeller performance. A total of 6 test

simulations were extracted to test the accuracy of the CFD results, including 6 different rotational speeds with the propeller in a hovering state. The results of the test simulations were compared to those of the ground test.

To be able to compare the accuracy of the calculations visually, two dimensionless coefficients were used. These coefficients were the thrust coefficient  $C_T$  and torque coefficient  $C_Q$ , and they are represented as follows:

$$C_T = \frac{T}{\rho A \Omega^2 R^2} \quad (5)$$

$$C_Q = \frac{Q}{\rho A \Omega^2 R^3} \quad (6)$$

where  $T(N)$  is the thrust of the propeller,  $Q(Nm)$  is the torque of the propeller,  $\rho$  is the local air density,  $A(m^2)$  is the rotor disk area, and  $\Omega(rad/s)$  is the rotational speed of the propeller.

The simulated results of the propeller thrust and moment at different rotational speeds are evaluated by the experimental results, as shown in [Fig. 13](#). The CFD results are displayed by solid graphs and the experimental results are displayed by hollow graphs. To make the comparison more intuitive, dimensionless coefficients (applying [Eq. \(5\)](#) and [Eq. \(6\)](#)) are used for plotting. It is easy to find that as the rotational speed increases, the moment coefficient keeps a constant value while there is a small rise in the thrust coefficient. Notably, the CFD method usually overestimates the thrust value and underestimates the torque value of small-scale propellers [17]. In this paper, the errors of the T-Motor  $13 \times 44$  propeller are less than 10.7 % and 8.3 % for the thrust value and torque value, respectively. When the propeller is in static condition, the accuracy of the prediction of the propeller thrust depends on the ability to capture the tip-vortex structure of the propeller blade. The results in this section show that the computational model and methodology used in this paper can sufficiently well predict the propeller thrust in a free environment.

## 4. Results and discussion

When propellers are hovering and there exists a ceiling overhead, the ceiling can turn the direction of the incoming flow and lead to changes in the performance of the rotors [19]. They are efficient in generating thrust due to the reduced downwash angle and changed pressure distribution of the upper rotor disk. However, when the plane of the rotor

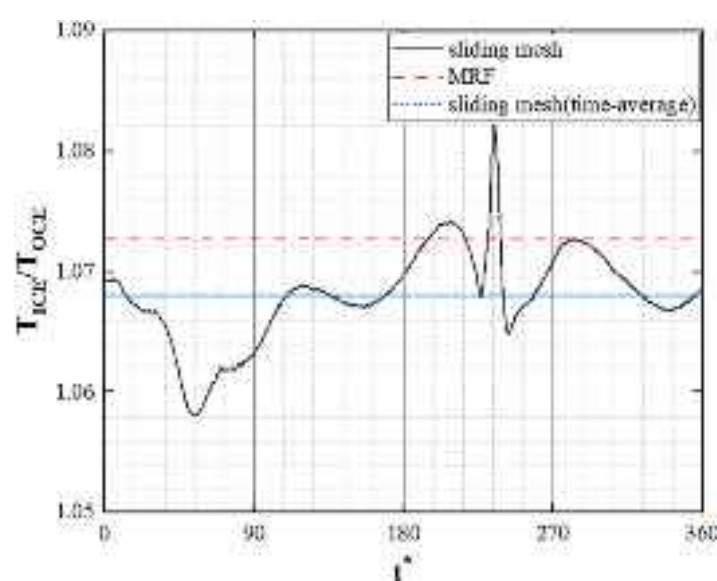


**Fig. 12.** Comparison of the MRF and sliding mesh method results of thrust ratio.

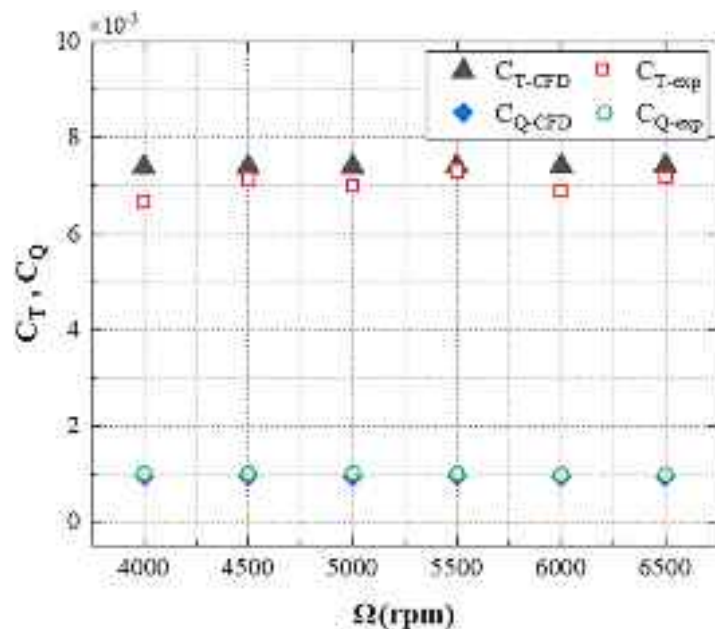


Fig. 13. Performance of the T-Motor 13 × 4.4 propeller at different rotational speeds.

disk is not parallel to the ceiling, the impact of the ceiling may cause significant asymmetry phenomena, mainly on the thrust that is not in the vertical direction and the torques that are not perpendicular to the plane of the rotor disk. In addition, changes in the thrust will be different from what it would have been without a tilt angle. In this section, the

influence of the ceiling on the aerodynamic characteristics of propellers with tilt angles is analyzed based on the MRF technique and ground test.

In Section 4.1, we compared the simulation results and experimental results of the propeller with tilt angles operating under a ceiling. In Section 4.2, we showed why the aerodynamic properties are generated

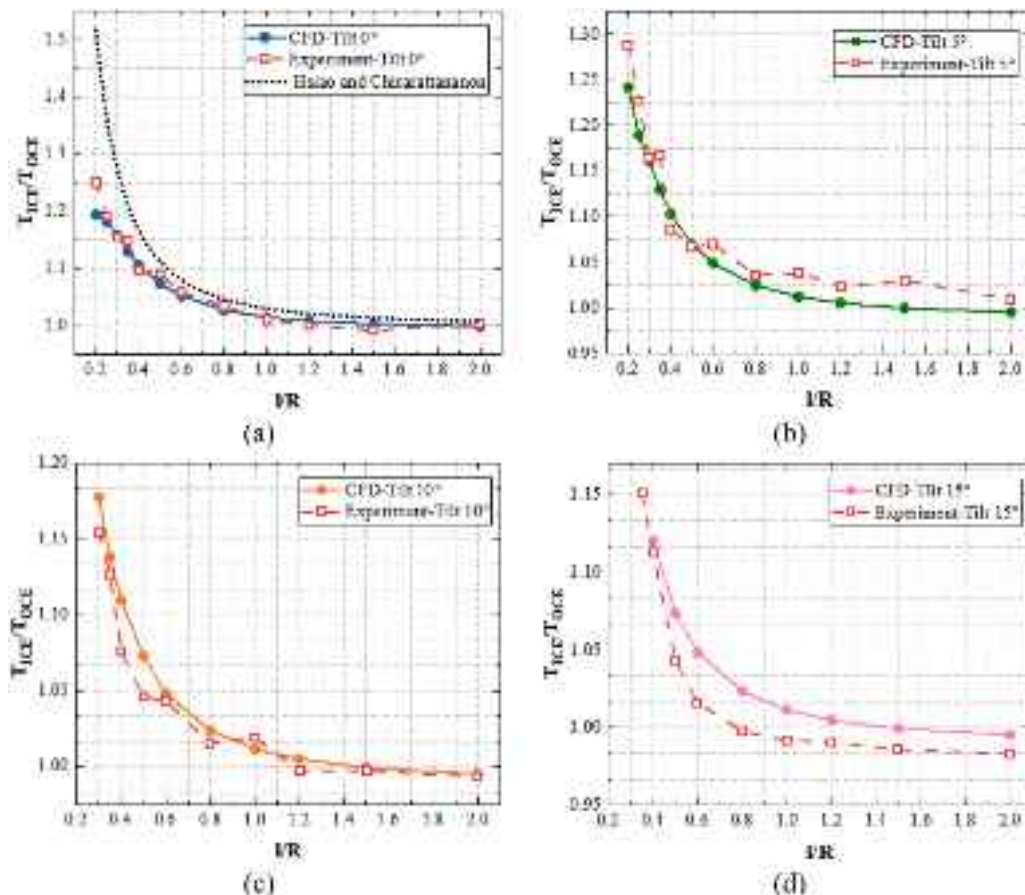


Fig. 14. Comparison of the experimental and computational results of thrust ratio.

by flow field visualization.

#### 4.1. Experimental validation of the cfd calculations

In this section, we selected four different tilt angles for the experiment and simulation and compared the results of the thrust. In the former procedure, the co-planar situation, where the rotor disk plane is parallel to the ceiling ( $\theta = 0^\circ$ ), and three different tilt angles ( $\theta = 5^\circ, 10^\circ, 15^\circ$ ) have been considered and analyzed. Moreover, twelve dimensionless distances between the center of the rotor disk and the ceiling ( $l/R = 0.2, 0.25, 0.3, 0.35, 0.4, 0.5, 0.6, 0.8, 1, 1.2, 1.5, 2$ ) were assessed. It is important to note that since the ceiling effect has a small area of influence and the blade may interfere with the ceiling, some angles cannot be investigated when the distance relative to the ceiling is quite small (eg :  $\theta = 10^\circ, l/R > 0.25$ ;  $\theta = 15^\circ, l/R > 0.3$ ). In addition, since the CFD method requires the presence of a certain space on the outside of the propeller as the rotational domain, the number of ground tests that can be carried out when the distance is extremely small will be greater than that of the simulations.

To compare the aerodynamic properties more intuitively when investigating the ceiling effect, the thrust ratio  $T_{ICE}/T_{OCE}$  is extensively used in later texts. The thrust ratio gives a quick indication of the percentage increase in thrust generated by the propeller when the ceiling is close. Fig. 14 displays the comparisons between the CFD and experimental results and shows how the thrust of the CFD and experimental results vary with the dimensionless distance  $l/R$ . For the case of the propeller parallel to the ceiling ( $\theta = 0^\circ$ ), the Hsiao and Chirarattananon model [25] of the ceiling effect is also plotted for comparison, and their model predicts the following:

$$\frac{T_{ICE}}{T_{OCE}} = \frac{1}{2} + \frac{1}{2} \sqrt{1 + \frac{1}{8z^2}} \quad (7)$$

The results in Fig. 14 show that the thrust of the propeller increases as it approaches the ceiling at all tilt angles. The experimental and simulation results match well. Although discrepancies exist between the experimental and CFD results because of the errors arising from both methods, they are considered acceptable within the range. Table 3 displays the percentage errors between the CFD and experimental results of the thrust of major cases mentioned at the beginning of this section. None of the errors exceeded 10.1 % indicating that the results are plausible. The CFD method overpredicts the thrust for all angles and distances.

With the simulation results, the curves show that the ceiling effect is negligible when  $l/R$  is greater than 1.2. The closest dimensionless distance to the wall is 0.2 for the angles of  $0^\circ$  and  $5^\circ$ . Correspondingly, the increases in thrust are 19.4 % and 24.1 % for these two closest cases. For the angle  $10^\circ$ , the minimum distance at which the CFD and ground tests both have been operated is 0.3R because of the interference of the blade with the ceiling plane for closer distances. For this distance and for angles of  $0^\circ, 5^\circ$ , and  $10^\circ$ , the total thrust of the rotor is increased by 15.9 %, 16 %, and 17.7 %, respectively. For the angle of  $15^\circ$ , the minimum distance increased to 0.4R. For this case, the thrust increases generated by the propeller for angles of  $0^\circ, 5^\circ, 10^\circ$  and  $15^\circ$  are 10.5 %, 10.3 %, 11 % and 12 %, respectively. From the results, it can be observed that an unexpected increase in lift occurs when the rotor with a tilt angle is in the region close to the ceiling effect. In contrast to the phenomenon of

reduced thrust when tilt angles exist between the rotors and the ground [17]. For the ceiling effect, when the distance is quite small ( $< 0.4R$ ), the existence of tilt angles between the propeller and the ceiling strengthens the thrust-increasing effect brought by the ceiling.

Considering the deviations that exist between the simulation and experimental results, errors may be introduced in both approaches. On the experimental side, there may be multiple reasons for the generation of errors in practice. For instance, the test bench was made of aluminum alloy profiles. Although the preparation of the pedestal was designed in detail, machining errors in the metal parts can cause each profile to not be standardized, which may lead to the possibility of error angles between the test and the floor and the wall. The tilt angles are adjusted by 3D printed connectors, (see Fig. 11) to minimize errors, and a 3D printer with high precision was chosen. However, due to the effects of temperature and light, there is still a possibility of deformation of the connectors. In addition, all the parts are linked by screws, and the stresses generated during the linking may cause some structural deformation. During the test, the adjustment of the distance from the ceiling to the rotor was realized manually, although multiple measurements were taken by utilizing a variety of devices, such as rulers and levels. This could lead to errors if at some distances the rotor is not parallel to the ceiling. The control board used to control the rotational speed of the rotor is based on feedback control and it is difficult to stabilize the rotational speed at a fixed value under real conditions. The speed usually fluctuates around the set value. This means the rpm value could not be the same as the value that we set in the simulations. Every test is conducted after a certain time to ensure that the motor has cooled. However, when the motor is working for a long time, there may be some deviations in the operation of the motor. The power supply used during the test could be sensitive to the test environment, and voltage instability can sometimes occur. Moreover, the propeller is placed on the test bench, which could create interference between the rotor and the bench. To evaluate the disturbance caused by the bench, three additional simulations were performed. A similar structure presented in Fig. 10 was built in the CFD calculations. Thrust value errors of less than 1 % for distances of  $0.5R, 0.6R$ , and  $1R$  have been found. Therefore, the interference caused by the test bench can be ignored. The simulation can never fully mimic the real environment, even though we consider the simulation in this paper to be realistic and reliable after a series of evaluations.

Beyond that, with regards to the CFD, the deviations are mainly due to the use of quasi-steady approximations. The MRF is a simplified model that cannot simulate the transient characteristics of the flow field but has excellent computational efficiency with considerable accuracy. In other research, this feature is also observed when the sliding mesh method results are compared. In all cases, the errors do not exceed 10.1 % for all the trust values under different conditions. Fig. 14 shows that the most significant error occurs in the case where  $l/R = 0.8, \theta = 15^\circ$ , and the error does not exceed 5 %.

In general, experimental tests cost more than simulations. Every connection needs to be designed, processed, and assembled on the test bench and every test requires many people to complete. For simulations, once the CFD method has been validated, batch calculations can be quickly performed under multiple similar working conditions. Furthermore, since propellers have strong unsteady characteristics and are sensitive to disturbances in the space environment, it is difficult to

**Table 3**  
Percentage errors between experimental data and CFD results.

Distance Angle	0.2	0.25	0.3	0.35	0.4	0.5	0.6	0.8	1
$0^\circ$	3.9 %	7.9 %	9.1 %	7.0 %	9.6 %	7.1 %	9.2 %	8.0 %	5.1 %
$5^\circ$	4.9 %	5.5 %	8.4 %	5.3 %	9.6 %	9.1 %	6.7 %	7.6 %	6.1 %
$10^\circ$	/	/	10.1 %	9.9 %	8.6 %	9.6 %	9.7 %	9.9 %	8.4 %
$15^\circ$	/	/	/	/	9.5 %	9.1 %	6.9 %	8.6 %	9.7 %

measure very accurate values through ground tests. As seen from Fig. 14 there exist some unreasonable oscillations in the experimental result curve, although the percentage error is not large and the overall trend is consistent with that of the CFD method. This may be caused by a variety of reasons mentioned above. Therefore, the experimental results are only used for verification, and the subsequent flow field analysis and modeling are carried out based on the CFD results.

#### 4.2. Flow field characteristics

Before modeling the ceiling effect of tilted propellers, it is necessary to analyze the characteristics of the flow from the data. The CFD method which has been validated in the previous section, has been used to analyze a series of cases with large ranges of  $\theta$  and  $l$ . Numerical simulations can be used to visualize the flow field and obtain details of asymmetric flow. Changes in the propeller performance originate from changes in the flow field stimulated by the rotor. The analysis in this paper was performed up to a tilt angle of 30°, since the scope of the ceiling effect is relatively small. When the angle increases above this value, the propeller needs to be positioned far away from the ceiling. At this time, the impact of the ceiling on the propeller is negligible and the thrust ratio is close to 1. For angles of 30°, 25°, 20°, 15°, and 10°, the minimum distances performed in simulations are 0.8R, 0.6R, 0.4R, and 0.3R, respectively since for close distances the rotational domain intersects with the ceiling.

The thrust ratios of the T-Motor '1344' propeller under ICE and OCE conditions for wide ranges of distances to the ceiling ( $l/R = 2, 1.5, 1.2, 1, 0.8, 0.6, 0.5, 0.4, 0.35, 0.3, 0.25, 0.2$ ) and inclinations ( $\theta = 0^\circ \sim 30^\circ$ ) are displayed in Fig. 15. The results of the classic ceiling effect model mentioned above is also shown in the figure as a solid line for comparison. At any tilt angle, the decrease in the distance between the rotor and ceiling results in an increase in the thrust ratio. The percentage increase in the thrust becomes progressively more significant as the propeller approaches the ceiling. The commonly used H-C model overestimates the thrust of the rotor in all cases. When the propeller is far from the ceiling ( $l/R > 0.6$ ), the thrust ratio  $T_{ICE}/T_{OCE}$  slightly decreases as the tilt angle increases. This result is expected and is the same as when propellers with tilt angles are in the ground effect region [17]. When the distance between the rotor and the ceiling decreases to 0.6R, although the thrust of the rotor with any tilt angle is smaller than that of the horizontal case, the thrust increases as the tilt angle increases. As the distance reduces to 0.5R, the thrust increases with higher tilt angles but exceeds the horizontal position only when the tilt angle is above 10°. Similarly, at distances of 0.4R and 0.35R, at the highest achievable tilt

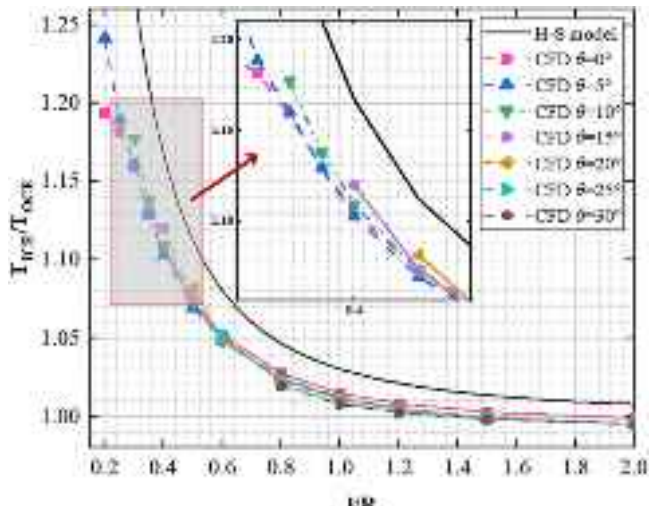
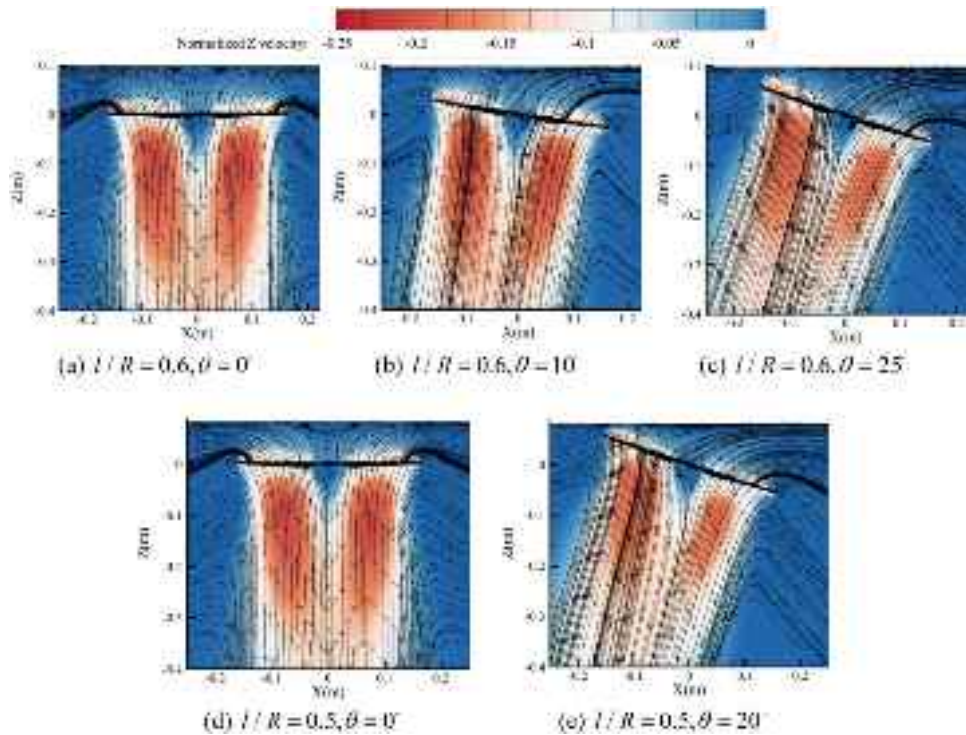


Fig. 15. CFD results of the thrust ratio.

angle for each distance, the thrust is higher than the value generated when the propeller is parallel to the ceiling at the same distance. As the rotor approaches the ceiling ( $l/R \leq 0.3$ ), the ceiling effect becomes stronger. In these cases, the existence of the propeller tilt angle causes an increase in the thrust, surpassing that of the horizontal conditions. The reasons for the physical phenomena that cause this change in the thrust with inclination, can be analyzed with the pictures below that present the velocity in the Z direction ( $m/s$ ) contours and vectors for some typical working conditions.

In the following analysis, we called the side of the rotor tip closer to the ceiling the upward side; in contrast, the side where the rotor tip is farther from the ceiling is called the downward side. Fig. 17 and Fig. 18 illustrate the velocity fields of different typical cases, where the Z velocity is normalized by the blade tip velocity. First, Fig. 16(a), (b) and (c) show the details of the flow under three different working conditions ( $\theta = 0^\circ, 10^\circ, 25^\circ$ ) with a distance of 0.6R. Since the propeller is close to the ceiling, the ceiling limits the direction of the incoming flow and changes its acceleration in the entrance region. The ceiling causes the air to flow radially, which reduces the inflow velocity and thus the downwash angle of the blade elements. When the rotor is parallel to the ceiling ( $\theta = 0^\circ$ ), an obvious ceiling vortex appears between the rotor and the ceiling in Fig. 16(a); this stagnant area will significantly affect the inflow velocity of the rotor disk. The affected area mainly covers the center of the rotor and the root of both blades. When the tilt angle increases, since the space between the upward blade and the ceiling decreases, the ceiling vortex gradually becomes unclear and moves towards the upward side blade, and the location of the stagnant area can still be determined by the intersection of the airflow flowing from both sides, as shown in Fig. 16(b) and (c). The existence of the tilt angle causes the airflow on the downward side to be sucked onto the upward blade. The influence region of the stagnant area gradually covers the part of the upward blade that mainly generates lift (Fig. 16(c)), resulting in a thrust at an angle of 25° greater than that at an angle of 10°. However, since the blade is still a short distance away from the stagnant area and the lift generated by the downward blade decreases, when tilt angles exist at a distance of 0.6R, the thrust is smaller than that in the horizontal case. In addition, the tilt angles deflect the propeller wake toward the downward side blade. Fig. 16(d) and (e) illustrate the velocity fields in the form of streamlines. Two cases are chosen for comparison since at this distance, the thrust when there is an angle of 20° exceeds the thrust when the rotor is parallel. When the distance is reduced to 0.5R and the tilt angle is 0°, the shape of the vortex remains unchanged, but the stagnant area is closer to the upper surface of the blades. Correspondingly, it has a wider impact on the inflow velocity of the upper surface of the rotor. As the tilt angle increases to 20°, similar to the case where the distance is equal to 0.6R, the stagnant area moves to the upward side of the blade and becomes completely on the upward blade, especially the part that contributes more to the thrust. In addition, due to the gap between the upward blade and the narrowing of the ceiling, the air inflow coming from the upward side direction is further restricted. The stagnant area is closer to the upward blade and the impact is stronger. Even though the downward blade is moving away from the ceiling, the thrust increase of the upward blade is greater than the decrease in the downward blade, resulting in the total thrust being greater than that in the parallel case.

Next, the cases in which the distances are  $l/R = 0.3, 0.2$  and the tilt angles are  $(0^\circ, 5^\circ, 10^\circ)$  and  $(0^\circ, 5^\circ)$  are analyzed. Fig. 17 presents the Z velocity contours and streamlines. The streamlines are depicted to illustrate the inflow structures. On the one hand, a small number of streamlines are drawn from a distant perspective; on the other hand, a larger number of streamlines are displayed to observe the vortex structures more clearly. In these cases, when the rotor has tilt angles, the thrust generated is greater than when the angle is zero. For a distance of 0.3R, as the gap decreases, the structure of the ceiling vortex changes. When the angle is zero, the two symmetrical vortices are squeezed into one vortex. At the same time, the stagnant area further expands,



**Fig. 16.** Visualization of the Z velocity contours and vectors for cases where the distances are relatively close.

covering almost 40 % of the radial position on both sides of the blade. When the tilt angle reaches 5°, the ceiling vortex can still be clearly observed. Similar to other cases of different distances, the vortex moves toward the upward side blade, causing the downwash speed of the upward blade to be changed more significantly. In addition, at such a distance, the wake of the upward blade is more severely sucked by the downward blade, especially for the case of  $\theta = 10^\circ$ . Although the tilt angle is not large, the wake flow fields show strong asymmetry. For the case in which the dimensionless distance reaches 0.2, the ceiling vortex is compressed so little that it is almost impossible to see. However, the area of influence reaches an unprecedented breadth. Most of the area of the blades is within the stagnant range, which greatly reduces the induced speed and causes a significant increase in thrust. When there exists a tilt angle of 5°, the influence on the downward side blade is almost unchanged, while the stagnant area covers almost the entire upward blade, resulting in a substantial increase in thrust.

Additionally, to further confirm the conclusions of the flow field analysis, we extracted the cross-section of the flow field 2.4 % R above the center of the rotor disk. This position is close enough to the upper surface of the propeller to reflect the inflow characteristics of the rotor disk. Fig. 18 shows the axial velocity component contours for several typical cases. In this figure, the upward blade is on the left. When the rotor is parallel to the ceiling, as the distance decreases, the area where the axial velocity exists gradually decreases. The area with high inflow velocity appears near the blade tip, and the high-speed area also decreases significantly as the distance between the rotor and the ceiling decreases. Considering the cases where the distance is 0.3R, as  $\theta$  increases, an asymmetry in the contour tends to be apparent. The inflow velocity near the upward blade is generally smaller than that near the downward blade, and the area with the highest speed is continuously compressed. In addition, the distribution of the inflow velocity near the downward blade is almost unchanged, which is why the total thrust increases when there exists a tilt angle for close distances. For the case of 0.2R, although the tilt angle is small, only five degrees, the high-speed area is also significantly compressed, resulting in a decrease in the induced velocity and larger thrust, similar to the 0.3R cases with tilt

angles. These conclusions are consistent with the flow field analysis results above.

Mainly, the changes in the induced velocity affect the changes in the propeller thrust. First, when there is no tilt angle, the flow field and inflow distribution are symmetrical, and a smaller gap distance will squeeze the ceiling vortex and cause the stagnation zone to be more influential. Then, the axial induced velocity decreases on the upward blade when the tilt angle increases. An opposite phenomenon appears on the downward blade. When the distance between the propeller and the ceiling is large ( $l/R > 0.5$ ), the increase in the inflow on the downward side is greater than the decrease on the upward side. However, as the gap decreases, the magnitude of the two influences on the two blades becomes opposite, especially when the upward blade is quite close to the ceiling. Indeed, a reduction in the axial induced velocity causes the local thrust to increase [21]. Consequently, the decrease in the induced velocity on the upward blade or the increase in the induced velocity on the downward blade depends on both the distance from the ceiling and the tilt angle. This is different from the conclusions of previous ground effect studies [17].

The analysis in this chapter reveals that the MRF method can predict the thrust of the propeller in the ceiling effect with tilt angles. It can also predict ceiling vortices, revealing the asymmetric characteristics of the flow, as in previous ground effect work [17]. Nevertheless, the MRF is a stationary approach, and it cannot be used to study the unsteady phenomena in the ceiling effects. The possible unsteady effects caused by the ceiling vortex still need to be studied with transient calculation methods.

#### 4.3. Results of the modified ceiling effect model

The nonlinear least squares algorithm with multiple variables is used to determine the three parameters in Eq. (4). The CFD results of T-Motor propeller- 13 × 4.4 are used to modify the model. The coefficients obtained from the application of the nonlinear least squares algorithm are  $a_0 = -6.8407$ ,  $a_1 = 1.6194$ ,  $b_1 = 7.2711$ , respectively. The completed equation is as follows:

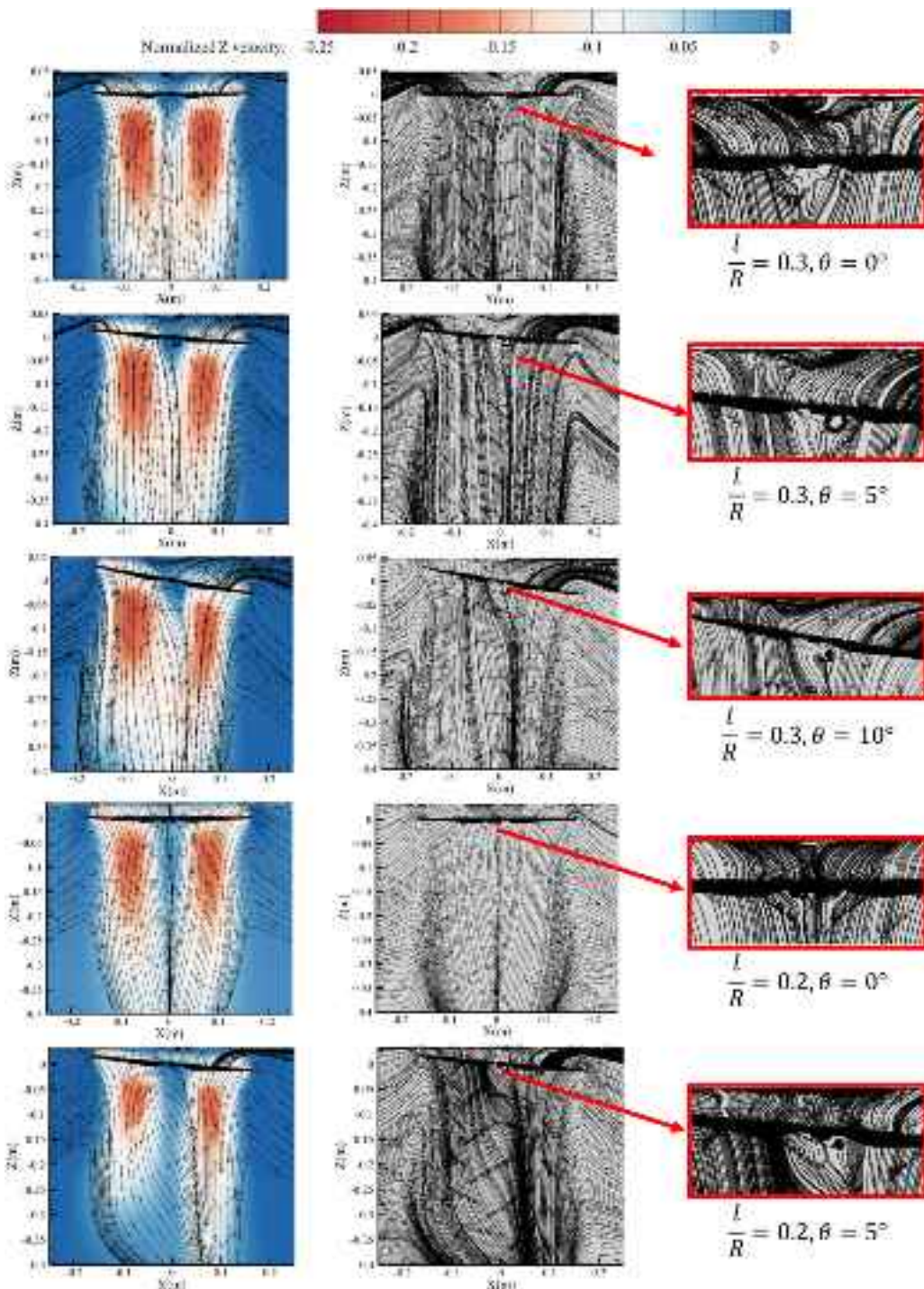


**Fig. 17.** Visualization of the Z velocity contours and vectors for cases where the distances are extremely close.

$$\frac{T_{ICE}}{T_{OCE}} = \frac{1}{2} + \frac{1}{2} \sqrt{1 + \frac{1}{8(l/R)^2} (-6.8407 + 1.6194\sin\theta + 7.2711\cos\theta)} \quad (8)$$

where  $l$  is the vertical distance between the ceiling plane and the center of the disk,  $R$  is the radius of the propeller,  $\theta$  is the tilt angle,  $T_{ICE}$  is the thrust when the propeller is affected by the ceiling, and  $T_{OCE}$  is the thrust when the propeller is not affected by the ceiling.

The model fits the data well with a correlation coefficient value of  $r$  equal to 0.99. Fig. 19 depicts the proposed model in the 3D representation. The model predicts the thrust ratio for angles between  $0^\circ$  and  $40^\circ$  with dimensionless distances ranging from 0.2 to 2.

The established model is evaluated below. Table 4 shows the errors of the CFD results and the values predicted by the proposed model of the thrust ratio. Fig. 20 illustrates the comparisons of the thrust ratio ( $T_{ICE}/T_{OCE}$ ) obtained by the proposed model and CFD results for non-dimensional distances of  $l/R = 0.2, 0.25, 0.3, 0.35, 0.4, 0.5, 0.6, 0.8, 1, 1.2, 1.5, 2$  and angles of  $\theta = 0^\circ, 5^\circ, 10^\circ, 15^\circ, 20^\circ, 25^\circ, 30^\circ$ . For the cases  $\theta = 0^\circ, 5^\circ, 10^\circ, 15^\circ$ , the experimental results are also taken into account. The largest errors occur at the distances closest to the ceiling, and in all cases, the errors are less than 6.5 %.

To verify the accuracy and general applicability of the model for different propellers with different shapes and sizes, 28 ground tests were

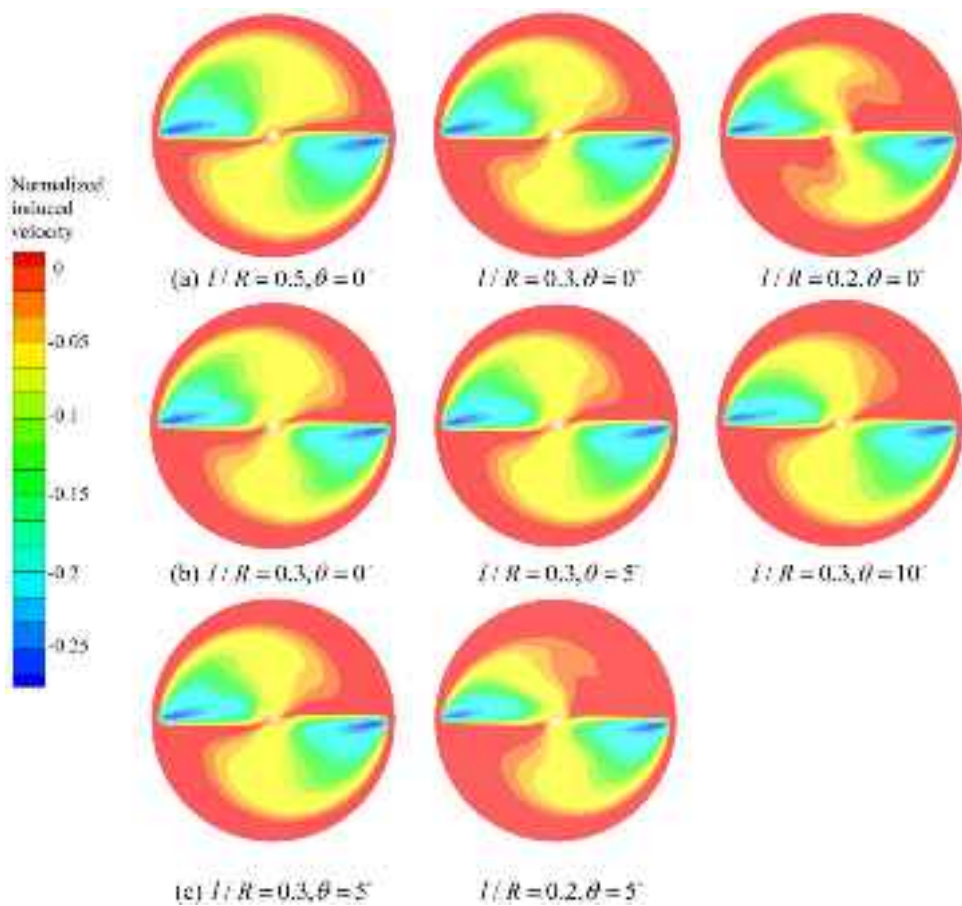


Fig. 18. Axial velocity component contours for typical cases.

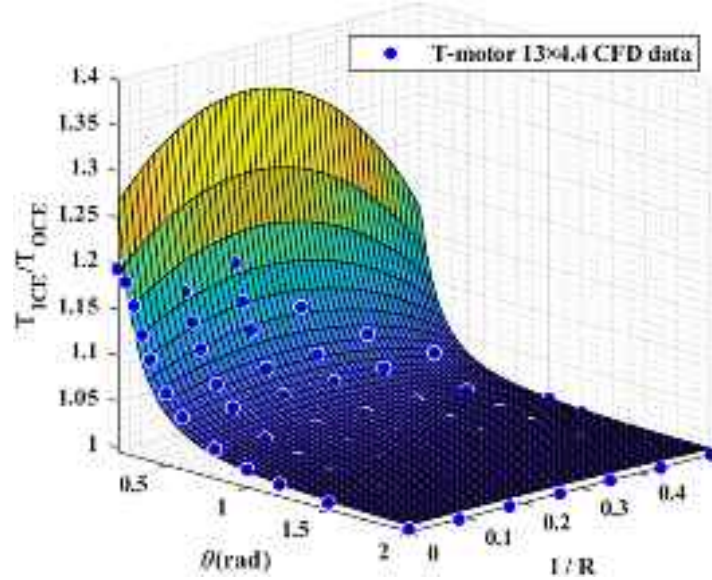


Fig. 19. 3D map of the proposed model.

carried out. Two other new propellers have been tested: APC 11 × 4.7 and T-Motor 10 × 3.3. For this analysis, we randomly selected some operating conditions within the range of the model for the experiment. Fig. 21 presents the distribution of the experimental results of the two propellers on the proposed model, and Table 5 and Table 6 show the errors of the experimental results and the values predicted by the

proposed model of the thrust ratio. The errors produced are all less than 5 %. The errors are listed in Table 5 and Table 6.

Overall, the model can be operated at angles from  $\theta = 0^\circ$  to  $40^\circ$  and a dimensionless distance of 0.2 to 2. For some close distance with large angles, although the model can predict the thrust ratios, the propeller will collide with the ceiling. However, this collision needs to be ignored.

**Table 4**

Errors of the thrust ratio of the T-Motor '13 × 4.4' propeller.

Dimensionless Distance	Tilt angle (°)	Error (%)	Dimensionless Distance	Tilt angle (°)	Error (%)
2	0°	0.5	0.5	10°	0.2
1.5	0°	0.3	0.4	10°	0.3
1.2	0°	0.1	0.35	10°	0.2
1.0	0°	0.2	0.3	10°	0.0
0.8	0°	0.7	2	15°	0.9
0.6	0°	1.5	1.5	15°	0.9
0.5	0°	2.1	1.2	15°	0.8
0.4	0°	2.5	1.0	15°	0.7
0.35	0°	2.6	0.8	15°	0.5
0.3	0°	2.3	0.6	15°	0.1
0.25	0°	0.0	0.5	15°	0.3
0.2	0°	6.0	0.4	15°	1.3
2	5°	0.9	2	20°	0.8
1.5	5°	0.8	1.5	20°	0.8
1.2	5°	0.7	1.2	20°	0.7
1.0	5°	0.5	1.0	20°	0.6
0.8	5°	0.1	0.8	20°	0.3
0.6	5°	0.3	0.6	20°	0.4
0.5	5°	0.5	0.5	20°	1.6
0.4	5°	0.5	2	25°	0.8
0.35	5°	0.5	1.5	25°	0.8
0.3	5°	0.2	1.2	25°	0.6
0.25	5°	2.8	1.0	25°	0.5
0.2	5°	6.4	0.8	25°	0.0
2	10°	0.9	0.6	25°	1.5
1.5	10°	0.9	2	30°	0.7
1.2	10°	0.8	1.5	30°	0.5
1.0	10°	0.7	1.2	30°	0.3
0.8	10°	0.5	1.0	30°	0.0
0.6	10°	0.1	0.8	30°	0.6

When the distance exceeds  $2R$ , the thrust ratio ( $T_{ICE}/T_{OCE}$ ) hardly changes.

## 5. Conclusions

Based on numerical simulations and experimental tests, the aero-

dynamic interferences of small-scale tilted propellers close to a ceiling were investigated in this paper. The flow characteristics in this condition are different from those of rotors hovering parallel to the ceiling. A wide range of tilt angles and ceiling distances ( $l/R$ ) were calculated and tested. Ground tests were conducted to preliminarily analyze the aerodynamic phenomena and evaluate the accuracy of the simulations. Finally, we proposed a ceiling effect model for tilted propellers by modifying Hsiao and Chirarattananon's model. The CFD results are in sufficiently good agreement, within a 10 % difference margin with the experimental results for the tilted ceiling effect. Therefore, a steady-state approximation can be used to obtain the thrust of a hovering propeller near a ceiling. The various costs of the computational methods are small compared to those of the ground experiment.

The results show that, in contrast to the phenomenon of reduced thrust when tilt angles exist between the rotors and ground, the existence of tilt angles in a tilted propeller hovering near a ceiling reduces the thrust when the dimensionless distance is large ( $l/R \geq 0.6$ ). When

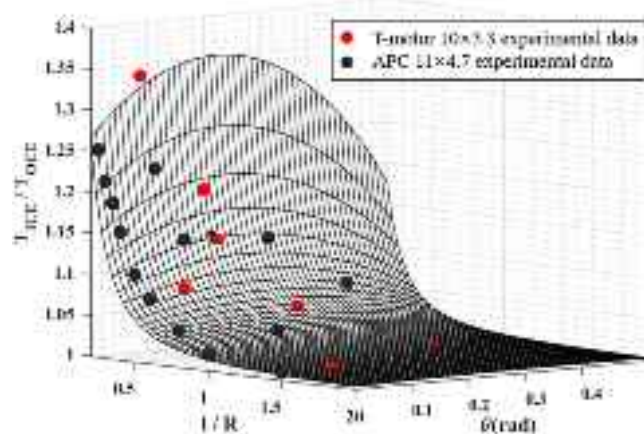


Fig. 21. Experimental results of the other two propellers on the 3D map of the proposed model.

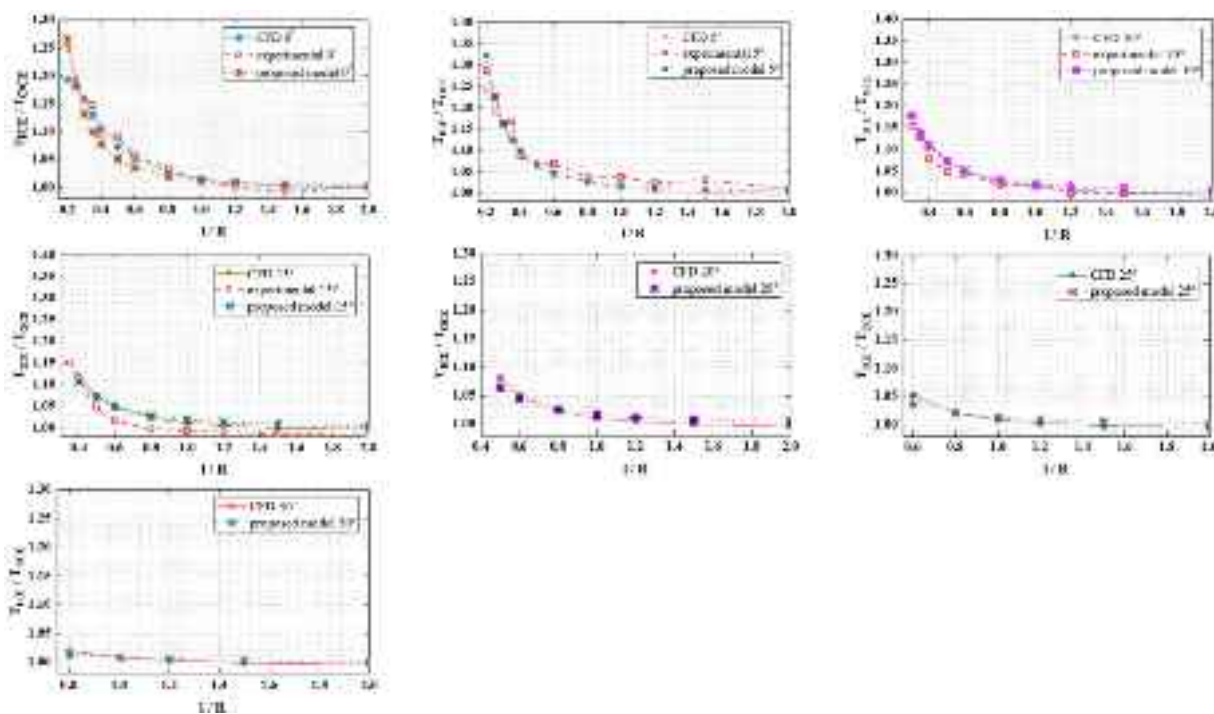


Fig. 20. Comparison of the thrust ratio achieved from the CFD method and proposed model.

**Table 5**

Errors of the thrust ratio of the APC '11 × 47' propeller.

Dimensionless Distance	Tilt angle (°)	Error (%)	Dimensionless Distance	Tilt angle (°)	Error (%)
1.5	0°	0.4	1.5	5°	0.3
1.2	0°	3.3	0.5	5°	4.3
1.0	0°	0.6	0.3	5°	4.1
0.8	0°	2.3	0.8	10°	0.7
0.6	0°	3.9	0.35	10°	0.2
0.5	0°	4.9	1.2	15°	3.4
0.4	0°	4.8	0.4	15°	3.0
0.35	0°	3.4	0.6	20°	2.9
0.3	0°	4.7	1.0	25°	1.1
0.2	0°	4.1			

**Table 6**

Errors of the thrust ratio of the T-Motor '10 × 3.3' propeller.

Dimensionless Distance	Tilt angle (°)	Error (%)
1.5	5°	0.7
0.5	5°	2.1
0.2	5°	1.4
0.8	10°	0.3
0.4	10°	2.7
0.3	10°	1.8
0.6	15°	0.2
1.2	20°	2.6
1.0	25°	2.9

the distance is small ( $0.4 \leq l/R \leq 0.5$ ), the total thrust increases when the tilt angle is sufficiently large ( $\theta \geq 10^\circ$ ). In particular, when the distance is small ( $l/R \leq 0.3$ ) the existence of tilt angles will increase the total thrust. These characteristics are also aligned with those of the presented flow field analysis. The axial induced velocity decreases on the upward blade when the tilt angle increases. An opposite phenomenon appears on the downward blade. When the distance between the propeller and the ceiling is large ( $l/R > 0.5$ ), the increase in inflow on the downward side is greater than the decrease on the upward side. However, as the gap decreases, the magnitude of the two influences on the two blades becomes opposite, especially when the upward blade is very close to a ceiling. Indeed, a reduction in the axial induced velocity causes the local thrust to increase. Consequently, the decrease in the induced velocity on the upward blade or the increase in the induced velocity on the downward blade depends on both the distance from the ceiling and the tilt angle. Moreover, the results of Hsiao and Chirattananon's model are compared with the CFD and experimental results, which showed good accuracy when the rotor is rotating parallel to the ceiling. However, regarding tilted rotors, the theory cannot be used to accurately predict the changes in the thrust. The proposed data-driven model can predict the thrust with the distance to the ceiling and angle inclination between the rotor and the ceiling with good accuracy.

In future works, the proposed model can be used in control laws when UAVs operate close to a ceiling. This has a certain significance for ensuring the safety and stability of drones. However, in our research, we did not consider the unsteady effects of the propeller in asymmetric cases. The aerodynamic characteristics in these cases will be much more complicated and require further investigation.

#### CRediT authorship contribution statement

**Yiliang Liu:** Writing – review & editing, Writing – original draft, Validation, Investigation, Formal analysis, Data curation, Conceptualization. **Zi Kan:** Validation, Supervision, Data curation. **Huadong Li:** Validation, Data curation. **Yuzhe Gao:** Validation, Data curation. **Daochun Li:** Supervision, Funding acquisition. **Shiwei Zhao:** Supervision, Funding acquisition, Conceptualization.

#### Declaration of competing interest

The authors declare that they have no known competing financial interests or personal relationships that could have appeared to influence the work reported in this paper.

#### Data availability

Data will be made available on request.

#### Acknowledgements

This work was co-supported by the National Natural Science Foundation of China [grant number T2288101, 52202430 and 92371201]; the National Key Research and Development Project [grant number 2020YFC1512500].

#### References

- [1] H. Li, Y. Liu, D. Li, et al., Ground test and numerical simulation of aerodynamic interference of the marsupial UAS, *Aerosp. 10* (2) (2023), <https://doi.org/10.3390/aerospace10020175>, 175, 2.
- [2] B. Theys, G. Dimitriadis, P. Hendrick, et al., Experimental and numerical study of micro-aerial-vehicle propeller performance in oblique flow, *J. Aircr. 54* (3) (2017) 1076–1084, <https://doi.org/10.2514/1.C033618>.
- [3] G. Cai, J. Dias, L. Seneviratne, A survey of small-scale unmanned aerial vehicles: recent advances and future development trends, *Unmanned Syst. 2* (02) (2014) 175–199, <https://doi.org/10.1142/S2301385014300017>.
- [4] A. Ollero, M. Tognon, A. Suarez, et al., Past, present, and future of aerial robotic manipulators, *IEEE Trans. Rob. 38* (1) (2021) 626–645, <https://doi.org/10.1109/TRO.2021.3084395>.
- [5] G.R. Spedding, P.B.S. Lissaman, Technical aspects of microscale flight systems, *J. Avian Biol.* (1998) 458–468, <https://doi.org/10.2307/36771165>.
- [6] B. Theys, G. Dimitriadis, T. Andrianne, et al., Wind tunnel testing of a VTOL MAV propeller in tilted operating mode. 2014 International conference on unmanned aircraft systems (ICUAS), IEEE (2014) 1064–1072, <https://doi.org/10.1109/ICUAS.2014.6842358>.
- [7] P. Sanchez-Cuevas, G. Heredia, A. Ollero, Multirotor aerodynamic effects in aerial manipulation, *Aerial Robotic Manipulation: Res., Dev. Appl.*, (2019) 67–82, [https://doi.org/10.1007/978-3-030-12945-3\\_5](https://doi.org/10.1007/978-3-030-12945-3_5).
- [8] S.L. Waslander, G.M. Hoffmann, J.S. Jang, et al., Multi-agent quadrotor testbed control design: integral sliding mode vs. reinforcement learning, in: 2005 IEEE/RSJ International Conference on Intelligent Robots and Systems. IEEE, 2005, pp. 3712–3717, <https://doi.org/10.1109/IROS.2005.1545025>.
- [9] T. Jardin, S. Proth, C.G. Magaña, Aerodynamic performance of a hovering microrotor in confined environment, *J. Am. Helicopter Soc. 62* (2) (2017) 1–7, <https://doi.org/10.4050/JAHS.62.022008>.
- [10] A. Betz, *The Ground Effect on Lifting Propellers*, 835, National Advisory Committee for Aeronautics, Washington, DC, USA, 1972. Technical report.
- [11] I. Cheeseman, W. Bennett, *The effect of ground on a helicopter rotor in forward flight*, ARC R&M (3021) (1955).
- [12] H. Xin, J. Prasad, D. Peters, et al., Ground effect aerodynamics of lifting rotors hovering above inclined ground plane, in: 17th Applied Aerodynamics Conference, 1999, p. 3223, <https://doi.org/10.2514/6.1999-3223>.
- [13] C. Paz, E. Suárez, C. Gil, et al., CFD analysis of the aerodynamic effects on the stability of the flight of a quadcopter UAV in the proximity of walls and ground, *J. Wind Eng. Ind. Aerodyn. 206* (2020) 104378, <https://doi.org/10.1016/j.jweia.2020.104378>.
- [14] X. He, K.K. Leang, Quasi-steady in-ground-effect model for single and multirotor aerial vehicles, *AIAA J. 58* (12) (2020) 5318–5331, <https://doi.org/10.2514/1.J059223>.
- [15] C. Pasquali, J. Serafini, G. Bernardini, et al., Numerical-experimental correlation of hovering rotor aerodynamics in ground effect, *Aerosp. Sci. Technol. 106* (2020) 106079, <https://doi.org/10.1016/j.ast.2020.106079>.
- [16] J.I. Milluzzo, A. Martinez, S. Drayton, et al., Experimental investigation of rotors hovering above inclined surfaces, *J. Am. Helicopter Soc. 66* (2) (2021) 1–11, <https://doi.org/10.4050/JAHS.66.022005>.
- [17] A. Garofano-Soldado, P.J. Sanchez-Cuevas, G. Heredia, et al., Numerical-experimental evaluation and modelling of aerodynamic ground effect for small-scale tilted propellers at low Reynolds numbers, *Aerosp. Sci. Technol. 126* (2022) 107625, <https://doi.org/10.1016/j.ast.2022.107625>.
- [18] F. Rovere, G. Barakos, R. Steijl, Safety analysis of rotors in ground effect, *Aerosp. Sci. Technol. 129* (2022) 107655, <https://doi.org/10.1016/j.ast.2022.107655>.
- [19] D.J. Carter, L. Bouchard, D.B. Quinn, Influence of the ground, ceiling, and sidewall on micro-quadrotors, *AIAA J. 59* (4) (2021) 1398–1405, <https://doi.org/10.2514/1.J059787>.
- [20] V.J. Rossow, *Effect of ground and/or ceiling planes on thrust of rotors in hover*. National Aeronautics and Space Administration, Ames Res. Center (1985).

- [21] Y. Luo, T. Ai, Y. He, et al., Aerodynamic analysis on unsteady characteristics of a ducted fan hovering in ceiling effect, *Eng. Appl. Comput. Fluid Mech.* 17 (1) (2023) 2196327, <https://doi.org/10.1080/19942060.2023.2196327>.
- [22] P.J. Sanchez-Cuevas, G. Heredia, A. Ollero, Multirotor UAS for bridge inspection by contact using the ceiling effect, in: 2017 International Conference on Unmanned Aircraft Systems (ICUAS). IEEE, 2017, pp. 767–774, <https://doi.org/10.1109/ICUAS.2017.7991412>.
- [23] S.A. Conyers, M.J. Rutherford, K.P. Valavanis, An empirical evaluation of ceiling effect for small-scale rotorcraft, in: 2018 International Conference on Unmanned Aircraft Systems (ICUAS). IEEE, 2018, pp. 243–249, <https://doi.org/10.1109/ICUAS.2018.8453469>.
- [24] Y.H. Hsiao, P. Chirarattananon, Ceiling effects for surface locomotion of small rotorcraft, in: 2018 IEEE/RSJ International Conference on Intelligent Robots and Systems (IROS). IEEE, 2018, pp. 6214–6219, <https://doi.org/10.1109/IROS.2018.8593726>.
- [25] Y.H. Hsiao, P. Chirarattananon, Ceiling effects for hybrid aerial–surface locomotion of small rotorcraft, *IEEE/ASME Trans. Mechatron.* 24 (5) (2019) 2316–2327, <https://doi.org/10.1109/TMECH.2019.2929589>.
- [26] B.B. Kocer, M.E. Tiriyaki, M. Pratama, et al., Aerial robot control in close proximity to ceiling: a force estimation-based nonlinear mpc, in: 2019 IEEE/RSJ International Conference on Intelligent Robots and Systems (IROS). IEEE, 2019, pp. 2813–2819, <https://doi.org/10.1109/IROS40897.2019.8967611>.
- [27] A.E. Jimenez-Cano, P.J. Sanchez-Cuevas, P. Grau, et al., Contact-based bridge inspection multirotors: design, modeling, and control considering the ceiling effect, *IEEE Robotics and Automation Lett.* 4 (4) (2019) 3561–3568, <https://doi.org/10.1109/LRA.2019.2928206>.
- [28] J. Hao, Y. Zhang, Z. Chao, et al., Aerodynamic performance of hovering micro revolving wings in ground and ceiling effects at low Reynolds number, *Chin. J. Aeronaut.* 36 (1) (2023) 152–165, <https://doi.org/10.1016/j.cja.2022.07.008>.
- [29] J. Cai, S. Gunasekaran, M. Ol, Effect of partial ground and partial ceiling on propeller performance, *J. Aircr.* 60 (3) (2023) 648–661, <https://doi.org/10.2514/1.C036974>.
- [30] R.W. Deters, G.K. Ananda Krishnan, M.S. Selig, Reynolds number effects on the performance of small-scale propellers, in: 32nd AIAA applied aerodynamics conference, 2014, p. 2151, <https://doi.org/10.2514/6.2014-2151>.
- [31] O. Gur, A. Rosen, Propeller performance at low advance ratio, *J. Aircr.* 42 (2) (2005) 435–441, <https://doi.org/10.2514/1.6564>.
- [32] E.V. Loureiro, N.L. Oliveira, P.H. Hallak, et al., Evaluation of low fidelity and CFD methods for the aerodynamic performance of a small propeller, *Aerosp. Sci. Technol.* 108 (2021) 106402, <https://doi.org/10.1016/j.ast.2020.106402>.
- [33] ANSYS, ANSYS FLUENT Theory Guide, ANSYS Inc., 2023.
- [34] ANSYS, ANSYS FLUENT User's Guide, ANSYS Inc., 2023.
- [35] H. Li, Z. Kan, D. Bie, et al., Aerodynamic interference analysis of multiple rotors in a heterogeneous unmanned aircraft system, *Phys. Fluids* 35 (11) (2023), <https://doi.org/10.1063/5.0174331>.
- [36] F.R. Menter, Two-equation eddy-viscosity turbulence models for engineering applications, *AIAA J.* 32 (8) (1994) 1598–1605, <https://doi.org/10.2514/3.12149>.
- [37] X. Liu, D. Zhao, N.L. Oo, Comparison studies on aerodynamic performances of a rotating propeller for small-size UAVs, *Aerosp. Sci. Technol.* 133 (2023) 108148, <https://doi.org/10.1016/j.ast.2023.108148>.
- [38] R.T.N. Chen, A survey of nonuniform inflow models for rotorcraft flight dynamics and control applications, *Euro. Rotorcraft Forum* (1989) A–89220.